# Ram to Scram Mode Transition in a Simulated Flight Acceleration

Ruixu ZHOU (周芮旭),[1,2] Fanzhao MENG (孟凡钊),[1,2] Tuo LI (李拓),[1,2] Zhongpeng LI (李忠朋),[1,2] and Huan LIAN (连欢)[*,2]

[1)]*School of Engineering Science, University of Chinese Academy of Sciences, Beijing 100049, China*

[2)]*State Key Laboratory of High Temperature Gas Dynamics, Institute of Mechanics, Chinese Academy of Sciences, Beijing 100190, China*

(*Electronic mail: hlian@imech.edu.cn)

(Dated: 26 April 2022)

Thrust abruption due to mode transition could be catastrophic for hypersonic vehicles. To understand the underlying physics, a direct-connected transient Flight Trajectory Simulator 1 (FTS-1) has been developed at the Institute of Mechanics, Chinese Academy of Sciences. This facility uses advanced high-speed measuring techniques, including thrust and static wall pressure measurement, and Schlieren and hydrocarbon radical chemiluminescence (CH* chemiluminescence) imaging. Kerosene fueled dual-mode combustor experiments are designed in an acceleration trajectory. The basic operation parameters, the flame and flow dynamics of the acceleration induced mode transition are evaluated. Discussions are given on the triggering mechanisms responsible for the ram to scram mode transition in a simulated flight acceleration.

## I. INTRODUCTION

Dual-mode scramjet (DMSJ) is one of the enabling technologies of Hypersonic air-breathing vehicles[1]. The introduction of an isolator and the modified design of the nozzle enable operation in a wide range of flight envelopes with Mach number and altitudes[2,3]. In order to meet the requirement of wide Mach number, the engine adjusts its working modes in correspondence to the flight envelope. When the flight Mach number is in the range of 3∼6, the engine normally operates in ramjet mode. The combustion in the combustor forms back pressure, which leads to upstream boundary layer separation and the formation of a thermal throat. The pseudo-combustion shock train propagates further upstream, sustains in the isolator and decelerates the mainstream to subsonic for the benefit of combustion efficiency. As the flight Mach number increases above 6, the engine may need to operate in scramjet mode for net positive thrust. Under scramjet mode, the shock train in the isolator dissipates gradually and the mainstream becomes supersonic, with sustainable combustion in supersonic flow.

Fuel mixing in DMSJ is closely related to the combustion heat released. The most common fuel injection method is transverse port injection. When the fuel is injected into the mainstream, complex flow structures are formed, which dominate the mixing process of fuel and oxidizer[4,5]. In the near field of fuel injection, mixing is achieved by large scale structures interactions that stretches the fuel-air interface steepens the local fuel concentration[4-6]. Downstream in the far-field of the injector, the mixing of fuel and air depends on both the turbulent mixing and mass diffusion. The main parameters that affect jet injection include the jet momentum flux ratio[7], injection angle[8], the fuel mass flow rate and boundary layers thickness[9], which determine the fuel spatial distribution, local equivalence ratio, and the sub-sequential combustion process.

Direct injection of fuel into the mainstream is difficult to achieve stable combustion, and may even cause combustion to be blown out[10]. In order to maintain stable combustion, three methods are commonly adopted to increase flame stability:

decreasing the flow mixing time, increasing the flow residence time and reducing the combustion chemical reaction time[3]. At present, the commonly used methods to increase the flow residence time includes cavity flameholder[11,12], strut[13] and backward step[14]. Among them, cavity flameholder is widely adopted in scramjet combustor due to its structural simplicity and advantages of low total pressure loss and local heat flux.

Combustion stabilization has been widely studied numerically and experimentally in literature. Previous studies systematically evaluate the effect of the combustion chamber configuration[15], incoming flow parameters[16,17], ignition process[18,19] and injection parameters[20,21]. The combustion stabilization has been summarized in four modes, including weak combustion, cavity shear-layer stabilized scramjet combustion, jet-wake stabilized ramjet combustion and the oscillation combustion modes between them[22-25]. The flame stability is governed by the coupling effects of the cavity recirculation strength and local stoichiometry[26-28], and the flow structure interactions between mainstream, jet, cavity shear layer, cavity recirculation zone and vortex structure[10,29]. Due to the nonlinearity of flame dynamics, small changes at the working boundaries, such as incoming flow conditions, injection conditions and wall temperature, may lead to flame stability transition under a specific working mode[10].

Despite the thorough study on the steady-state performance of DMSJ covering aspects from fuel mixing to ignition and combustion stabilization, studies on the transient combustion behavior are sparse in literature due to the absence of transient operation facility and large transient computational expense. Previous transient studies mainly focus on the inlet unstart caused by combustion-induced pressure abruption, accompanied by the upstream displacement or "disgorging'" of the original inlet shock system[30,31]. The experimental simulation of the back pressure is usually achieved by mechanical throttling instead of combustion due to difficulties in experimental realization. Transient characteristics of inlet unstart have been experimentally studied by mechanical throttling which induces controllable back pressure. Wieting[32] conducted ex-

periments in 1976 to study the unstart boundary by adding a cylindrical pin downstream of the inlet of a model scramjet engine. It has been found that the inlet unstart phenomenon can be analytically modeled by normal and oblique shock theory. Rodi Emami et al.[33] studied the engine unstart oscillation characteristics with a moving flap. The time-resolved pressure measurement was taken and oscillation at 300 Hz has been observed after the inlet unstart. Wagner et al.[34] also studied the engine unstart oscillation characteristics with a moving flap and suggested a strong connection between the unstart and boundary-layer separation. Combustion-induced back pressure has been achieved by hydrogen heat addition in the model combustor. Shimura et al.[35] and O'Byrne et al.[36] increased the hydrogen to air equivalence ratio experimentally and observed strong combustion oscillation of the wall pressure and thrust measurement prior to the inlet unstart. Laurence et al.[31] performed experimental and numerical investigation of the transient fluid-combustion phenomena. The primary mechanism responsible for unstart has been concluded to be the overloaded thermal choking and local boundary-layer separation. Transient combustion studies have been focusing on combustion response to abruption of equivalence ratio and wall temperature[37]. In addition, the DMSJ performance during transient vehicle acceleration and deceleration has been obtained solely from flight test. Specifically, the transient characteristics of mode transition during acceleration and deceleration have not been studied neither experimentally nor numerically. In order to understand the transient flow behavior and foster a novel design of flight envelope, a direct-connected transient Flight Trajectory Simulator 1 (FTS-1) has been constructed at the Institute of Mechanics, Chinese Academy of Sciences. The facility is detailed in the next section and is capable of simulating the flight trajectory with simultaneously varying the total pressure, temperature[38,39] and Mach number[40].

In this paper, we studied the transient characteristics of mode transition during a simulated flight acceleration. Firstly, ramjet and scramjet working modes are identified from the static pressure measurement based on the classical one-dimensional analysis. Abruption in thrust has been observed due to mode transition during the acceleration process. Secondly, the steady-state flow and flame dynamics are evaluated based on the pressure measurements, high-speed Schlieren and hydrocarbon radical chemiluminescence (CH* chemiluminescence) imaging. Imaging processing techniques are developed to extract the crossflow penetration characteristics. The steady-state characteristics are quantified by Proper Orthogonal Decomposition (POD). Transient evolution of the heat released, shock train strength and fuel crossflow characteristics are specially analyzed with discussions on the physics of mode transition during acceleration.

## II. EXPERIMENTAL SETUP

### A. EXPERIMENTAL FACILITY

The experiment was carried out in the direct-connected transient Flight Trajectory Simulator 1 (FTS-1) at the Institute of Mechanics, Chinese Academy of Sciences. The direct-connected transient Flight Trajectory Simulator 1 (FTS-1) consists of the compressed gas supply system, a water-cooled hydrogen burning vitiator specifically designed with wide operating range, a water-cooled variable throat De Laval nozzle, the testing section and the integrated control system. The novel design of the wide range vitiator enables the flight altitude simulation in terms of corresponding total pressure and temperature. The flight speed simulation is achieved by the variable throat De Laval nozzle, of which a cam module is integrated and torqued by an accurately controlled servo motor unit. The schematic of the FTS-1 is illustrated in Fig. 1. The FTS-1 is capable of simulating flight envelopes within the altitude of 20-30km and the Mach number of 4.5-6.5. The heated gas flow rate of FTS-1 is up to 3kg/s, and the total pressure and temperature are up to 4Mpa and 1900K. The transient flight trajectory simulation requires careful synchronization of each sub-system. The mass flow rates of the air, hydrogen, oxygen and nitrogen are synchronized and timed considering the dynamic response of each individual PID feedback controlled pressure regulating valve. The throat area of the De Laval nozzle is adjusted to the vitiator mass flow rates accordingly. The timing sequence of a typical transient flight simulation is shown in Fig. 2. The air pressure in the vitiator is stabilized for approximately 6.0s before the oxygen injection at 11.0s which ensures the oxygen-enriched environment when the hydrogen is introduced in the vitiator at 12.5s. The small hydrogen torch is turned off at 14.0s when self-sustainable combustion has been established in the vitiator. The flight trajectory simulation starts at 14.5s when the pilot hydrogen and sub-sequential fuel injection in the scramjet combustor model are initiated. The mass flow rate of air, oxygen and hydrogen and the De Laval nozzle throat area are adjusted from 14.5s to 24.5s accordingly. The nitrogen and hydrogen exchange is timed from 24.5s to 30.0s as a safety precaution. Figure 3 shows the measured vitiator total pressure during a typical acceleration experiment. The detailed experimental parameters are summarized in Table I.

Figure. 4 shows the detailed schematic diagram of the test section. The test section contains a constant area isolator a the cross-section of 80 mm x 40 mm and a model combustor, which is a single side expansion with an inclination of 2° and equipped with double cavity flameholders. The two cavities have the same size, and the first cavity is located 447 mm downstream of the inlet of the isolation section. The length, depth and the angle of the trailing edge of the cavities are 65 mm, 17 mm and 22.5° respectively. The kerosene injection block and the pilot hydrogen injection block are installed at 60.5 and 9.5 mm upstream of the cavity respectively, where the kerosene spray block has a row of 6 injection ports of 0.3mm. The spark plug ignition, marked as a red five-pointed star in Fig. 4, is installed at the bottom of the first cavity. In
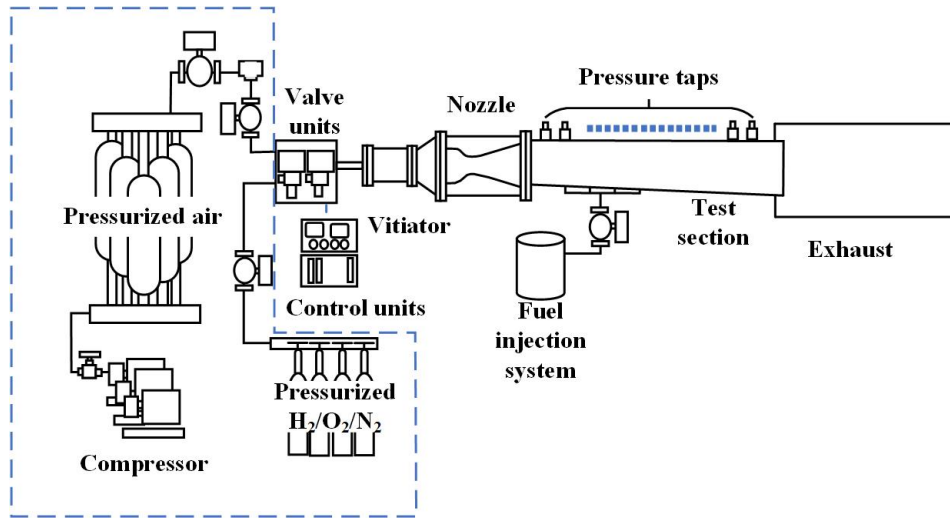
FIG. 1: Continuous variable Mach number direct-connected supersonic combustion test facility.

TABLE I: Experimental parameters

| Simulated flight Mach number | Simulated flight altitude /km | Simulated dynamic pressure /kPa | Simulated total pressure /kPa | Simulated total temperature /K | Total flow of heating gas /(g·s$^{(-1)}$) | Kerosene flow /(g·s$^{(-1)}$) |
|---|---|---|---|---|---|---|
| $5.0 \sim 6.0$ | $20.99 \sim 26.28$ | $82 \sim 50$ | $1548 \sim 1939$ | $1249 \sim 1648$ | $1878 \sim 1178$ | $\approx 28$ |
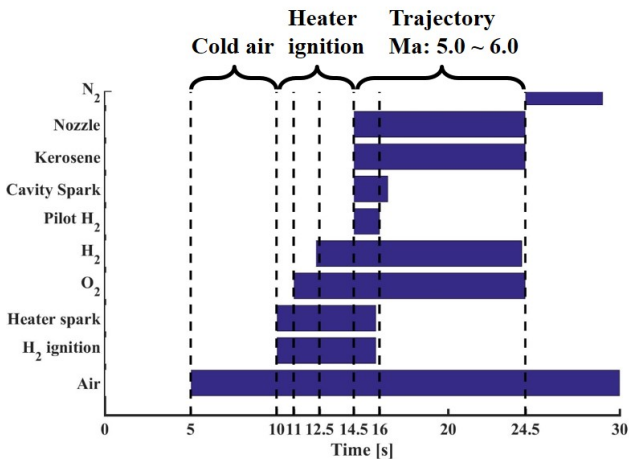


FIG. 2: Timing sequence of the transient experimental gases.



FIG. 3: Total pressure of the transient operation heater.

addition, a pair of quartz glass windows are installed on both sides of the first cavity for the flow and combustion field visualization which occurs in the red dashed box in Fig. 4.

**B. DIAGNOSTIC TECHNIQUES**

The thrust sensor Omega LC203-500 with a sampling frequency of 1kHz is mounted between the sliding frame at the front of the text facility and the ground support. The thrust 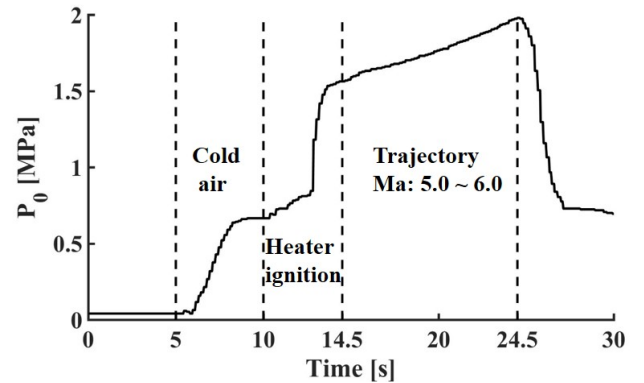induced by the burned fuel heat addition can be obtained by subtracting the thrust of the vitiator calibration. The pressure acquisition system is the combination of pressure gauges at 100kHz and 300Hz. The 100kHz pressure sensors, marked as blue dots in Fig. 4, are Kulite XTL-190(M) with a measuring range of 0.7MPa. The 300Hz low-frequency pressure sensors are installed at the upper part of the model combustor and connected to the DTC Initium acquisition system via a copper pipes. A band-pass filter is installed in front of the high-speed camera Phantom v2612 to capture the CH* chemiluminescence signal for combustion visualisation. The center wavelength of the filter is 430nm, with a bandwidth of 10nm and a peak transmittance of 0.882. The camera exposure time is $20 \ \mu s$ at the frame rate of 6000 frames per second and
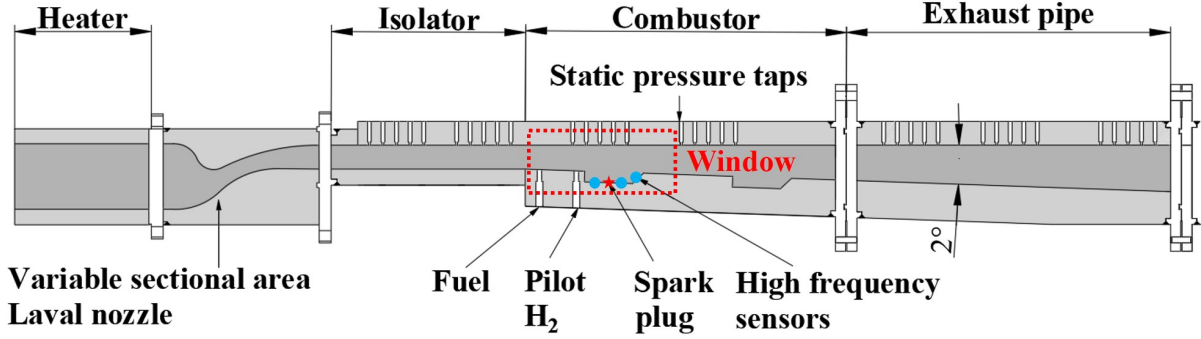
FIG. 4: Detailed schematic diagram of the test section.

the resolution of 1280 pixels x 800 pixels. Flow field visualization is acquired by the traditional z-type Schlieren system. The Schlieren system camera has an exposure time of 2 $\mu s$, a frame rate of 6000 frames per second and a resolution of 1920 pixels x 700 pixels. Two Stanford DG645 signal delay generators are used to trigger and synchronize the measurement systems. The trigger DG645 is externally triggered by a TTL signal from the control room and then triggers each acquisition system in sequence. The synchronization DG645 is used as the external clock of the two imaging cameras.

## III. DATA PROCESSING

### A. FLAME EXTRACTION

The CH* chemiluminescence signal intensities have been found to be positively related to the heat release[22,41]. Therefore, the spatial dispersion of CH* chemiluminescence represents the spatial evolution of the heat released in the combustor. In order to extract the CH* chemiluminescence intensity in the presence of digital bipolar impulse noise (salt and pepper noise), a simple extraction method has been developed. In this paper, the analysis of the heat release rate is evaluated based on the proposed processing method. The flow chart of quantitative extraction of heat release from the flame CH* chemiluminescence is illustrated in Fig. 5. The three steps process includes pre-processing, denoising and flame intensity extraction. The pre-processing takes care of void images due to transient flame blowout. After the pre-processing process, the CH* chemiluminescence images are de-noised following the first proposed method. A mean filter with a size of 3 x 3 is used to smooth the salt and pepper noise in the images. Then, Otsu method[42] is used to binarize the blurred images. This method categorizes the image into foreground and background according to the threshold value, and calculates the variance between different categories:

$$\sigma_w = W_f \sigma_f^2 + W_b \sigma_b^2 \qquad (1)$$

Where $W$ represents the probability of a class, $\sigma$ represents class variances and subscripts "$f$", "$b$" represent foreground

and background respectively. After processing by the Otsu method, a binary image is obtained, in which 1 represents the chemiluminescence coordinate and 0 represents the case of invalid void pixel.

The above process generates a set of coordinates, and the CH* intensities at those coordinates in the original image are used for heat release representation. This method has the advantage of maintaining intensity information from the original CH* images.

### B. JET EXTRACTION

The cross-flow fuel injection forms a complex vortex structure. In ramjet mode, the cross-flow jet acts as aerodynamic throttling in addition to the fuel mixing process and is usually characterized by the longitudinal penetration depth. In scramjet mode, liquid fuel breaks from the liquid column into small blocks and droplets along the flow direction, and its primary breakup distance is usually used to characterize the mixing characteristics. These two important quantities of fuel jet can be derived from the Schlieren images. Hence, we propose a two-step method to quantitatively extract the jet penetration depth and the liquid length of its primary breakup distance, as shown in Fig. 6. The two-step method includes de-noising and iterative boundary detection. The de-noising process is consistent with the flame extraction process detailed in Fig. 5. A traditional textbook iterative boundary detection method has been adopted to detect the upper boundary and the downstream liquid breakup point. The upper boundary and the liquid breakup point are used to quantitatively define the jet penetration depth and the liquid length.

### C. PROPER ORTHOGONAL DECOMPOSITION

The POD is one of the most widely used techniques in analyzing fluid flow velocity which performs linear decomposition and extracts elastic modes in terms of their contribution to the kinetic energy of the system[43–45]. In our case, the scalar
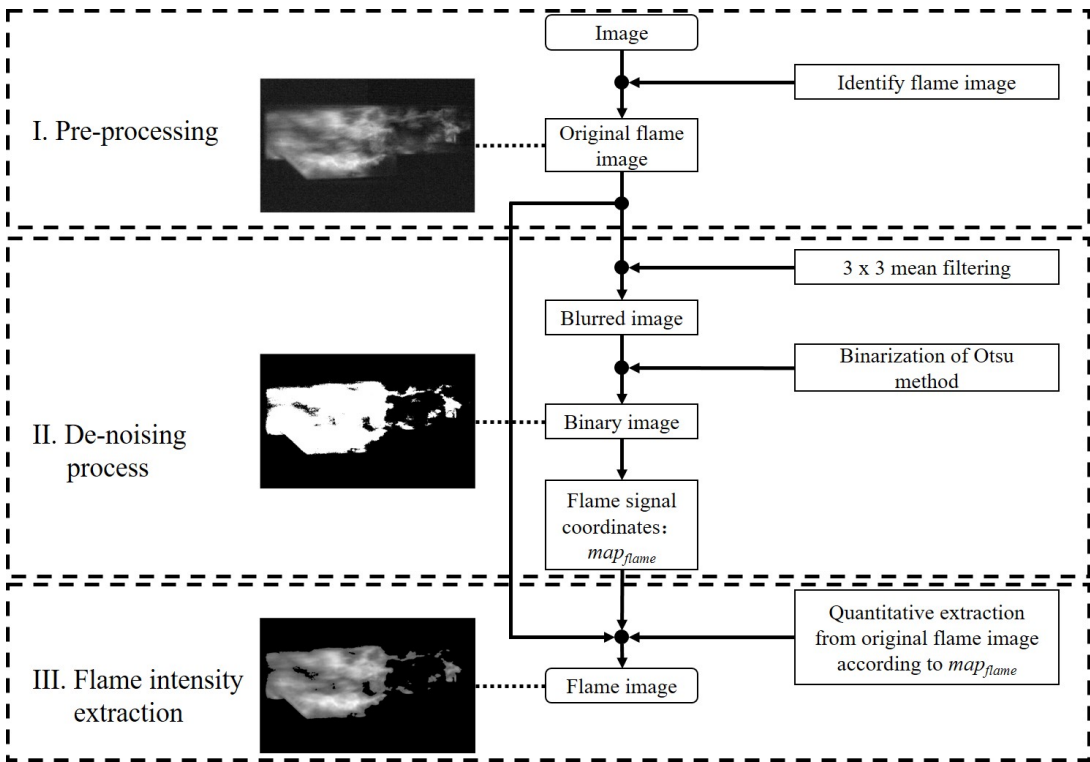
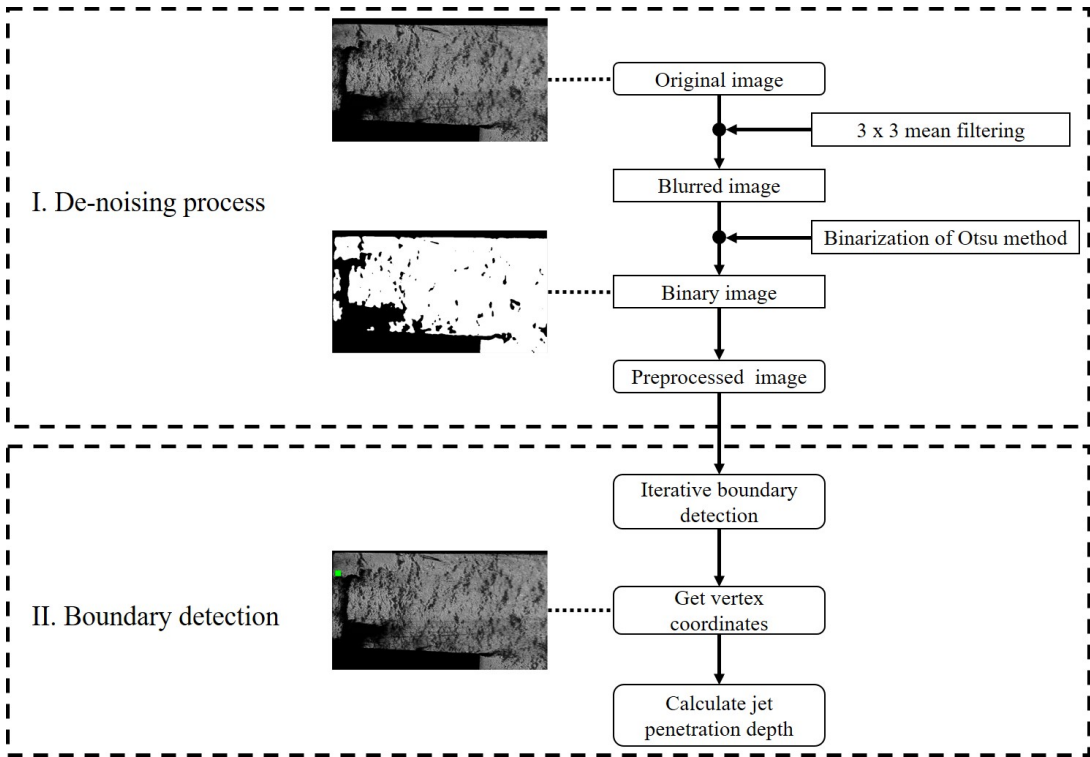FIG. 5: Flow chart of flame heat release quantitative extraction.



FIG. 6: Flow chart of jet penetration depth quantitative extraction.

quantity is the two-dimensional CH* chemiluminescence intensity extracted from the images with the method detailed in the previous section. The two-dimensional CH* chemiluminescence intensity positively correlates to the heat addition. Thus the POD method can be adopted in the case of flame analysis and extracts combustion modes in terms of their contribution to the heat release of the system. The instantaneous two-dimensional scalar can be reformed as a one-dimensional vector of $S$, and the matrix of $S^{(k)}$ further introduces the temporal dimension in the scalar vector. The vectorized $S$ with the dimension of $[1, i \times j]$ and its temporal evolution $S^{(k)}, [k, i \times j]$ are expressed as follows.

$$S = [x_{1,1}, x_{1,2}, ..., x_{1,j}, ...x_{2,j}, ...x_{i,j}]^T \quad (2)$$

$$S^{(k)} = \begin{bmatrix} x_{1,1}^{(1)} & x_{1,2}^{(1)} & \cdots & x_{1,j}^{(1)} & x_{2,j}^{(1)} & \cdots & x_{i,j}^{(1)} \\ x_{1,1}^{(2)} & x_{1,2}^{(2)} & \cdots & x_{1,j}^{(2)} & x_{2,j}^{(2)} & \cdots & x_{i,j}^{(2)} \\ \cdots & \cdots & \cdots & \cdots & \cdots & \cdots & \cdots \\ x_{1,1}^{(k)} & x_{1,2}^{(k)} & \cdots & x_{1,j}^{(k)} & x_{2,j}^{(k)} & \cdots & x_{i,j}^{(k)} \end{bmatrix} \quad (3)$$

The Proper Orthogonal Decomposition (POD) performs linear decomposition of $S^{(k)}$ by finding a series of orthonormal basis functions $\varphi_m$ and its corresponding coefficients $c_m^{(k)}$, which is resolved by minimizing the following equation.

$$S^{(k)} = \sum_{m=1}^{M} c_m^{(k)} \varphi_m \quad (4)$$

$$\sum_{k=1}^{K} \| S^{(k)} - \sum_{m=1}^{M} c_m^{(k)} \varphi_m \|^2 \to min \quad (5)$$

The minimization problem is solved by constructing a symmetric matrix of R as follows, where R is proportional to the square of the intensity of CH* chemiluminescence.

$$R = \frac{1}{k} S^{(k)} S^{(k)T} \quad (6)$$

The symmetric matrix $R$ is equivalently expressed by its eigenvalue $\lambda_m$ and coefficients $c_m$.

$$Rc_m = \lambda_m c_m \quad (7)$$

Since the intensity of CH* chemiluminescence is positively related to the heat release rate, the POD of the vectorized two-dimensional CH* chemiluminescence intensity S is a useful tool to understand the regions where the majority of combustion heat releases and disperses. By sorting the real non-negative eigenvalues $\lambda_m$ in descending order $\lambda_1 > \lambda_2 > \cdots > \lambda_M > 0$, where the summation of $\lambda_m$ equals 1, the corresponding mode matrix $\varphi_m$ representing the square of the intensity of CH* chemiluminescence can be obtained by projecting S onto the coefficients $c_m$, which is sorted in the order of importance in terms of capturing the heat release of the system.

## IV. RESULTS AND DISCUSSION

In this section, the ram and scram modes are identified from the measured pressure distribution. The Mach number distribution is calculated based on the one-dimensional analysis. Methods to identify the working modes are detailed in references[30,46,47]. Qualitative observation and quantitative evaluation of the transient flow and flame dynamics during a typical acceleration experiment are presented based on the high-speed Schlieren and CH* images.

### A. BASIC OPERATION CHARACTERISTICS

The thrust measurement during acceleration is shown in Fig. 7. At 21.809s, a thrust abruption is observed with a sudden decrease of around 200N, which accounts for 66% of the total thrust. Since the fuel mass flow rate has been kept as constant, the equivalence ratio is varied only by incoming flow variation. The result shows that under certain conditions, the acceleration-induced flow variations could result in thrust abruption, which could be disastrous for engine control and flight safety. The ram and scram modes are identified based on the measured static wall pressure distribution and the Mach number distribution calculation following the quasi-1D analysis of Heiser and Pratt[30].
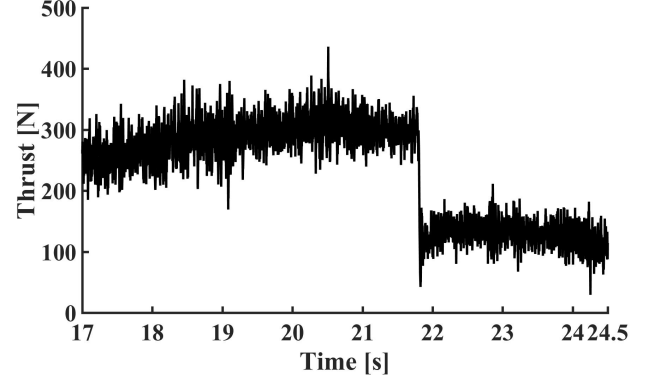


FIG. 7: Time history of the thrust.

The Mach number $M_a$ is calculated based on the following equation:

$$\frac{dM_a}{dx} = M_a[\frac{1 + \frac{(\gamma-1)M_a^2}{2}}{1 - M_a^2}] \times [-(\frac{1}{A}\frac{dA}{dx}) + \frac{1 + \gamma M_a^2}{2}(\frac{1}{T_t}\frac{dT_t}{dx})] \quad (8)$$

where $A$, $x$, $\gamma$, $T$ represent the cross-section area of the test section, the axial distance from the isolator entrance, and the specific heat ratio, temperature of the mainstream, respectively. The $dT_t/dx$ in Eqs. (8) means the change of the total temperature along axial distance, which is a function of $dA/dx$, $dP/dx$, $dM_a/dx$ and $M_a$

$$P(x) = P_{in} \frac{A_{in}}{A(x)} \frac{(M_a)_{in}}{M_a(x)} \sqrt{\frac{T(x)}{T_{in}}} \tag{9}$$

$$T(x) = T_{in} \frac{T_t(x)}{(T_t)_{in}} \left[ \frac{1 + \frac{(\gamma-1)(M_a)_{in}^2}{2}}{1 + \frac{(\gamma-1)M_a^2(x)}{2}} \right] \tag{10}$$

where $p$ represents the pressure of the mainstream, and the subscript "in" represents the parameters at the isolator entrance. From the stream-wise wall pressure distribution measurement, the corresponding Mach number is evaluated following Eqs. (8) to Eqs. (10). It should be pointed out that there are numerical errors rooting from the time discretization process, so that the discretized Mach number calculation during acceleration are analyzed together with the high-speed Schlieren and CH* images for physical understanding.

The 3D time-space evolution of the pressure distribution and the corresponding Mach number is shown in Fig. 8 and Fig. 9. $P_1$ represents the entrance pressure of the isolator. The black plane in Fig. 9 represents when the Mach number equals one. An increase in the wall static pressure has been observed upstream of the first cavity where the Mach number decreases below unity, which indicates that the pseudo-combustion shock train has been generated from heat addition and remains sustainable in the isolator. Hence the combustor is identified as ramjet mode. The equivalence ratio increases continuously during the acceleration process due to flow variation, while the shock train system is stable during the ramjet mode. This means that during the ramjet mode, a transient balance has been established between the heat addition and flow variation in the combustion chamber, resulting in a stationary shock train in the isolator. However, further acceleration breaks the pressure balance and leads to the mode transition from ramjet to scramjet. The pseudo-combustion shock train develops from oblique shock wave to dissipation and the whole flow path becomes supersonic, as shown in Fig. 9 when the combustor is considered to work in scramjet mode. In addition, Fig. 8 shows that the mode transition occurred at around 21.750s indicated by a large pressure drop, which is slightly earlier than the time of 21.809s given for the instant of thrust abruption. This is because the pressure drop is caused by the movement of the pseudo-combustion shock train, and the sudden change of thrust occurs after the pseudo-combustion shock train disappears, which will be discussed later, so the sudden change of thrust is later than the pressure drop time.

Quantitative analysis of the heat release is given by integrating the spatially distributed intensity signals of CH* chemiluminescence images. The defined $I_{total}$ is a direct representation of combustion heat addition assuming a positive correlation between the CH* chemiluminescence intensity and the heat released. The absolute value in Fig.10 is the integral of CH* intensity normalized by the CH* intensity at 17.0 s.

$$I_{total} = \sum_{i=1}^{R} \sum_{j=1}^{C} I_{i,j} \tag{11}$$
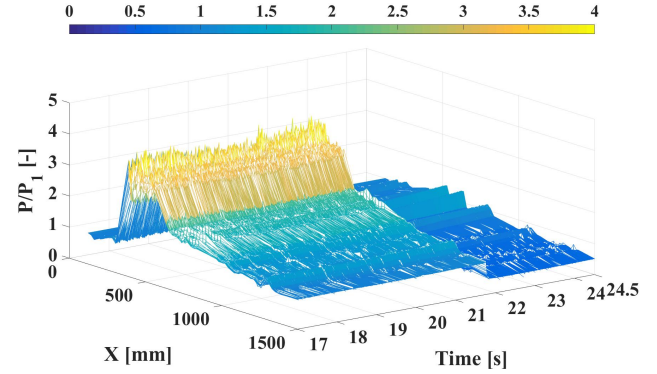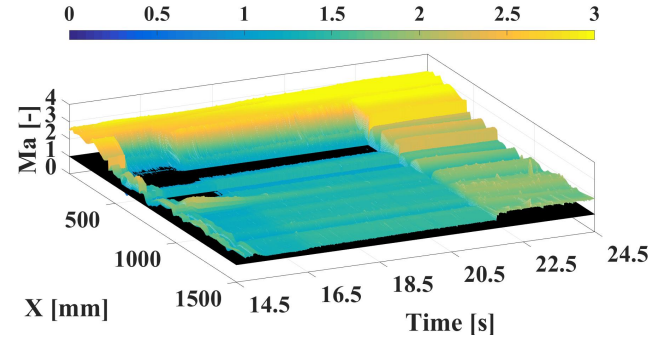


FIG. 8: Time-space of pressure distribution.



FIG. 9: Time-space of Mach distribution.

where $I_{i,j}$ represents the intensity value at row I and column J of CH* chemiluminescence, R and C represent the total number of rows and columns respectively. Fig. 10a shows the time series of the integrated CH* chemiluminescence intensity representing the heat released. Generally, the heat released under the ramjet mode shows an ascending trend and appears to be consistent under the scramjet mode during the simulated flight acceleration. The temporal evolution of the probability of $I_{total}$ in each $0.5s$ window is given in Fig. 10b. It is quite obvious that the heat released at the ramjet mode is significantly higher than that of the scramjet mode. Under the ramjet mode, the pdf spread of the heat release is about four times that of the scramjet mode, suggesting strong combustion oscillation under the ramjet mode.

To summarize, for the current experiment, ramjet mode occurs from 14.5s-21.5s and is followed by mode transition between 21.5s to 22.0s. Sustainable scramjet mode is from 22.0-24.0s until the end of the simulated acceleration at 24.5s. Acceleration-induced thrust abruption is observed first time from the ground experiment during mode transition at 21.809s. The 2D projection of the pressure distribution is shown in Fig. 11 to illustrate the timeline. In the following sections, 19.5s-21.5s and 22s-24s are selected with an interval of 0.5s for the evaluation of the ramjet and scramjet characteristics. Special focus is given to the transient mode transition characteristics between 21.750s to 21.765s.
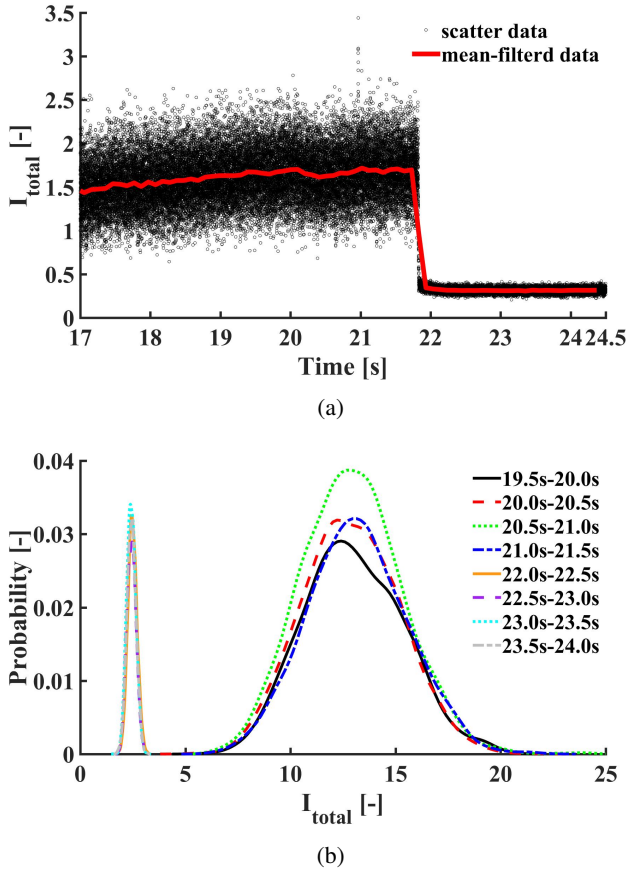
(a)



(b)

FIG. 10: Transient characteristics evolution, time history of (a) $I_{total}$ and (b) corresponding probability distribution during 19.5s-21.5s and 22.0s-24.0s.
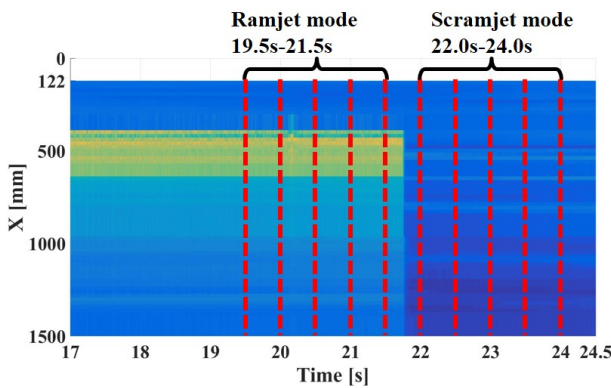


FIG. 11: Time selection of ramjet mode and scramjet mode.

## B.  FLAME DYNAMICS DURING ACCELERATION

Figure 12 is an example of the instantaneous high-speed Schlieren and CH* images during acceleration. $t = 17s, t = 19s$ and $t = 21s$ shows the three characteristic stages of the ramjet mode. while $t = 23s$ shows the flame and flow characteristic of the scramjet mode. During the ramjet mode,

the pseudo-combustion shock train in the combustor decelerates the mainstream to subsonic. For $t = 17s, t = 19s$ and $t = 21s$, the kerosene crossflow jet distributes the kerosene fuel droplets into the mainstream and modulates the flow. A vortices circulation zone is formed at the jet wake, and intense combustion occurs in this area and cavity shear layer. It should be noted that although the pseudo-combustion shock train consistently remains in the form of oblique shock until ramscram mode transition between 21.740s to 21.770s, the fuel distribution characteristics are quite different with variations. This is most likely to be caused by the three-dimensional shock wave and crossflow mixing layer interactions. The nonreactive multi-phase physics is already complex in nature, the heat addition from combustion further complicates the phenomenon. Based on the image processing method detailed in the previous section, attempts are given to provide quantitative evaluations to understand the transient acceleration process.

As mentioned above the POD method can be adopted on the CH* chemiluminescence high-speed images for flame analysis which extracts combustion modes in terms of their contribution to the heat release of the system. If the eigenvalues are sorted in descending order, the corresponding POD modes are arranged in the order of contribution. The contribution percentage can be quantified by normalizing over the total summation of eigenvalues. Fig. 13a shows the normalized POD eigenvalues. It can be seen that the first two eigenvalues and POD modes contribute to more than 15% of the system energy of both ramjet and scramjet operation, suggesting the presence of strong coherent flow structures which enable stable combustion. For higher order combustion modes, the normalized POD eigenvalues appear to be consistent for both ramjet and scramjet operation which could indicate similar flow dynamics in the inertia and dissipative range. Fig. 13b illustrate the cumulative performance of the combustion modes. For the first 100 combustion modes, the first-order derivative of the cumulative normalized POD eigenvalues of the ramjet operation is slightly higher than that of the scramjet operation. This could be caused by the presence of stronger coherent vortex structures in ramjet operation. For high order combustion modes beyond 100, the first-order derivative of the cumulative normalized POD eigenvalues of the scramjet operation is higher than that of the ramjet operation. This indicates that the scramjet operation is possibly more sensitive to the dissipative flow structures and prone to minor fluctuations.

The first two combustion modes are chosen to characterize the stabilization in the following section. As the incoming Mach number increases, the pseudo-combustion shock train maintains the form of oblique shock at the ramjet operation. The formation of the two combustion zones is related to the interaction between the three-dimensional shock wave and the crosssflow jet splitting phenomenon. Under ramjet mode during 19.5s-21.5s, the temporal averaged CH* chemiluminescence high-speed images are plotted in comparison with the POD combustion modes in Fig. 14. The main stable combustion zone of ramjet mode can be divided into jet wake combustion and cavity shear layer combustion zone, marked as 1 and 2 respectively. The upper beam of kerosene jet of high penetration depth induces coherent structures downstream of
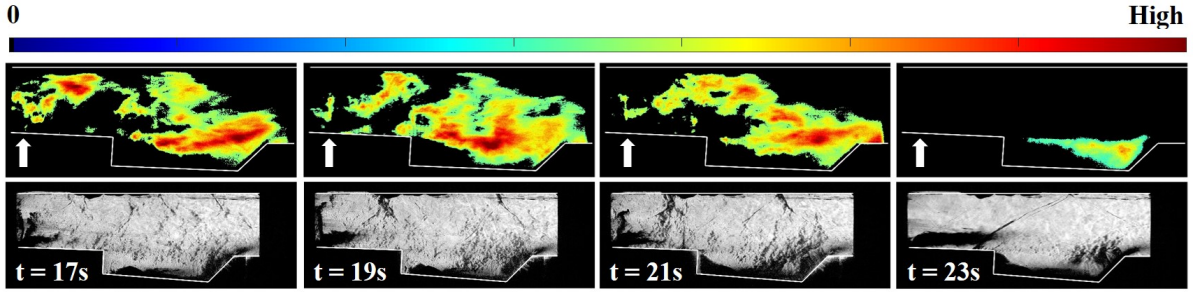
FIG. 12: Flow field and combustion field during acceleration process.
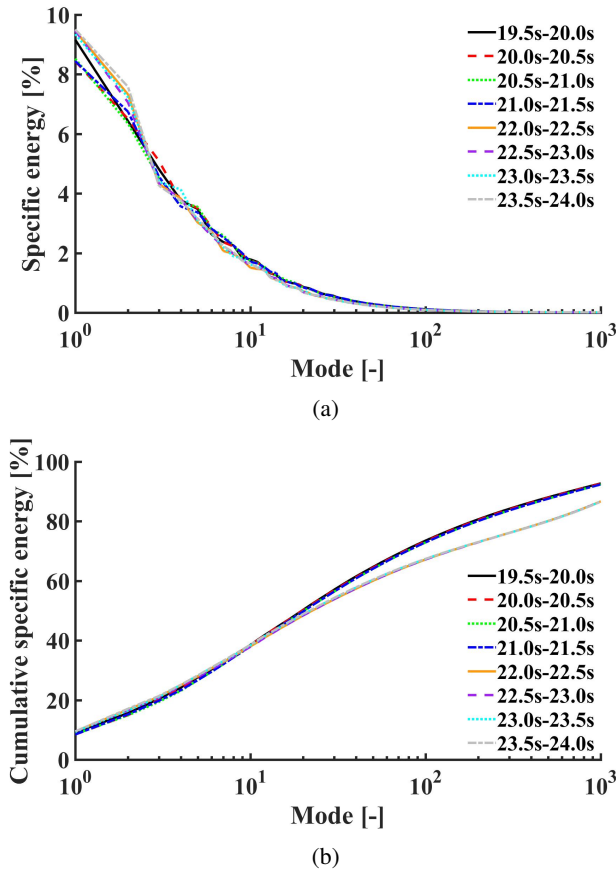


(a)



(b)

FIG. 13: POD linear decomposition during 19.5s-21.5s and 22.0s-24.0s : (a) POD eigenvalues in descending order (b) Cumulative POD eigenvalues.

the crossflow jet and enables jet wake combustion. The other beam of lower penetration depth forces the kerosene into the boundary layer and results in cavity shear layer combustion. In addition, while the flame in the jet wake propagates downstream, part of the flame, marked with dashed lines, enters the entrainment region of the cavity. As the mainstream flow accelerates, transportations between the energy-containing regions are observed, suggesting the temporal evolution of turbulent coherent structures under ramjet acceleration.

The jet wake stabilized zone is presumed categorized as partially premixed flame. The cavity stabilized flame is considered to be premixed. The flame spreading angle of premixed cavity stabilized flame during acceleration is calculated from the CH* chemiluminescence high-speed images and shown in Fig. 15. The temporal average of the cavity stabilized flame has been taken in the window of 0.5s from 19.5s to 21.5s. Since the fuel mass flow rate has been kept constant, it is quite clear that under the ramjet mode the mainstream flow acceleration is responsible for the ascending mainstream flow velocity ($U$) and the flame spreading angle ($\theta$) as defined in Fig. 15a[48]. As a consequence, the flame propagation rate ($S_T$) orthogonal to the flame surface increase due to both the mainstream acceleration and the acceleration-induced flow transportation.

Under scramjet mode during 22.0s-24.0s, the temporal averaged CH* chemiluminescence high-speed images are plotted in comparison with the POD combustion modes in Fig. 16. The scramjet mode mainly corresponds to the shear layer cavity stabilized combustion as shown in area 1 in the temporal averaged images. The first mode of POD shows two energy-containing regions suggesting the presence of coherent flow structures. Different from the ramjet mode acceleration, there is little temporal evolution of the turbulent coherent structures under scramjet mode.

As illustrated in Fig. 17, the flame spread angle is near constant, suggesting stable flow structures. This finding is consistent with the POD analysis under scramjet mode. With the ascending mainstream flow velocity ($U$) and the steady flame spreading angle ($\theta$), the flame propagation rate ($S_T$) orthogonal to the flame surface increase purely due to the mainstream acceleration.

To summarize, POD analysis and flame spread angle identification of the CH* chemiluminescence high-speed images are performed. Physical understandings of the two methods are consistent. Significant temporal evolution of turbulent coherent structure is observed under the ramjet mode, which is induced by acceleration-cavity interaction. The flame spreading angle ($\theta$) positively correlates to the mainstream flow velocity ($U$), suggesting the increase of flame propagation rate ($S_T$) is due to both the mainstream acceleration and the acceleration-induced flow transportation. The flame dynamics are characterized by jet wake, cavity stabilized combustion and in-between combustion oscillations. Different from
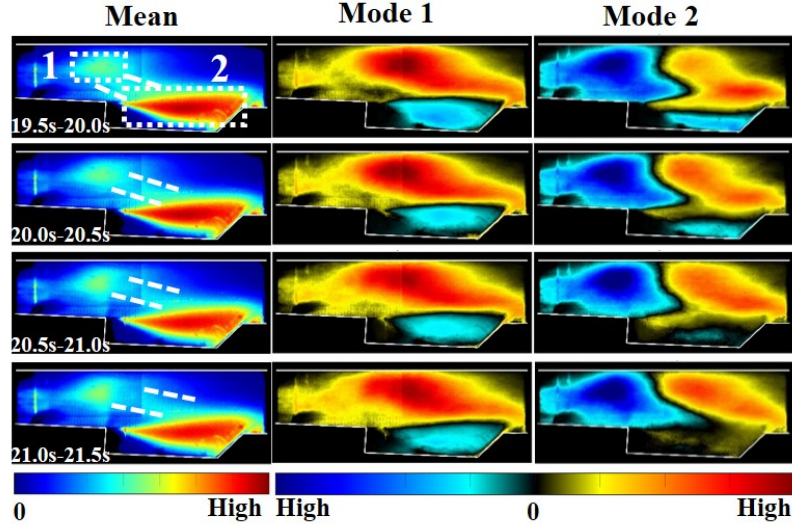
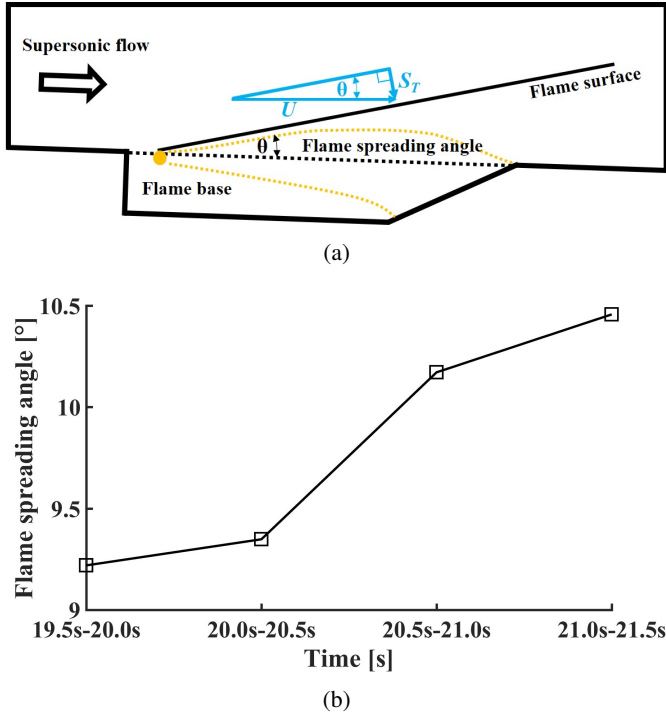FIG. 14: The temporal average and the first two POD modes under ramjet mode during 19.5s-21.5s.



(a)



(b)

FIG. 15: (a) Illustration of the flame propagation rate ($S_T$), the mainstream flow velocity ($U$), and the flame spreading angle ($\theta$)[48], and (b) Flame spreading angle under the ramjet mode (19.5s-21.5s).

the ramjet mode acceleration, there is little temporal evolution of the turbulent coherent structures under the scramjet mode. The flame spread angle ($\theta$) is near constant, suggesting the flame propagation rate ($S_T$) is purely governed by the mainstream acceleration ($U$). The flame dynamics is characterized as shear layer cavity stabilized combustion with little oscilla-

tion.

## C. FLOW DYNAMICS DURING ACCELERATION

The instantaneous Schlieren images of ramjet mode (from 19.5s-21.5s) and scramjet mode (from 22.0-24.0s) are shown in Fig. 18. The flow dynamics of the two working modes have been mainly summarized as the pseudo-combustion shock train and supersonic core flow by researchers over the past two decades. In addition, the fuel jet crossflow structure governs the mixing and sub-sequential combustion process. Thus, the pseudo-combustion shock train and crossflow fuel jets' performance in simulated acceleration are discussed in detail in this section.

The leading edge of the pseudo-combustion shock train is traditionally quantified based on static wall pressure and it-s derivative. Visual observation or pattern recognition image processing of the high-speed Schlieren shadowgraph images have also been used for identifying shock train structures by the community. Hutzel et al.[49] compared six pressure-based methods defining the leading edge of the pseudo-combustion detection with high-speed shadowgraph images. The pressure ratio has been considered to be the most suitable method to represent the shock leading edge due to its simplicity and high accuracy. Therefore, the pressure ratio between the static wall pressure and the pressure at the isolator entrance is adopted in the paper to define the leading edge of the pseudo-combustion shock train. A ratio of 1.5 is used as the defined threshold. In addition, the pressure ratio between the isolator and the combustor entrance is a direct representation of the shock train intensity. However, this method does not consider the streamwise dependence. Thus, the pressure spatial partial derivative is used here to define the pseudo-combustion shock train intensity.

The pressure spatial partial derivative $\frac{\triangle p}{\triangle x}$ is defined as
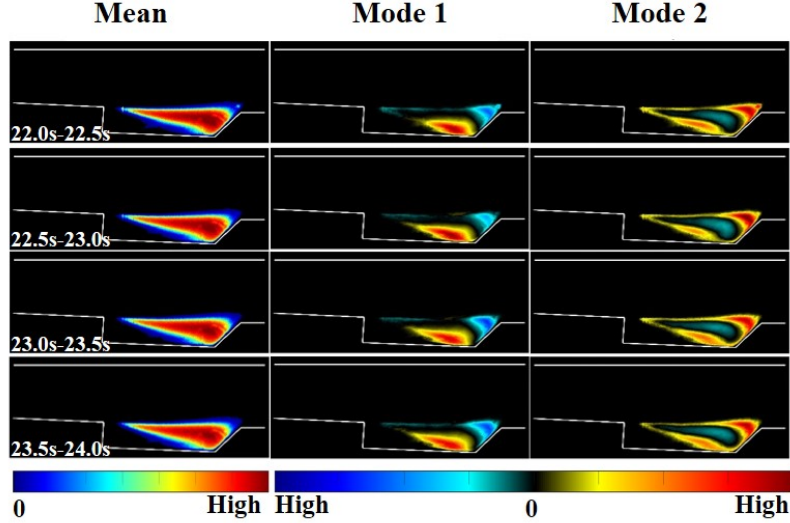
FIG. 16: The temporal average and the first two POD modes under scramjet mode during 22.0s-24.0s.
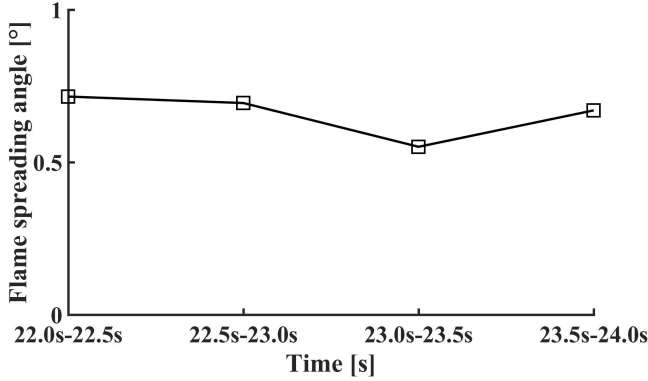


FIG. 17: Flame spreading angle under scramjet mode.



FIG. 18: Instantaneous Schlieren images during 19.5s - 21.5s and 22.0s - 24.0s.

$$\frac{\triangle p}{\triangle x} = \frac{P_2 - P_{LE}}{x_2 - x_{LE}} \qquad (12)$$

where $P$, $x$ represent the pressure ratio and axis position, and the subscripts "2" and "LE" represent isolator exit and the defined shock train leading edge. The pressure derivative quantifies the intensity of the pseudo-combustion shock train. As illustrated in Fig. 19, the leading edge of the pseudo-combustion shock train system maintain around 320mm downstream of the isolator entrance under ramjet mode. During mode transition, the leading edge quickly moves downstream and disappears. The shock train intensity decreases as the flow accelerates, suggesting a normal to oblique shock train evolution as shown in Fig. 20.

As the pseudo-combustion shock train decays and dissipates, the interaction between the crossflow transverse fuel jets and the shock wave has been observed from the Schlieren images. The fuel jet penetrates into the crossflow providing f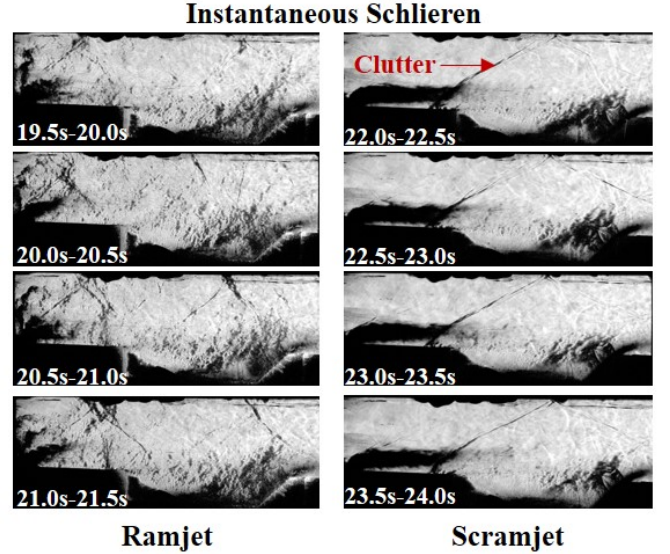low blockage and air throttling to the incoming flow, hence generating a three-dimensional bow shock structure whose strength depends on the level of air throttling blockage and the intensity of the pseudo-combustion shock train. Since the intensity of pseudo-combustion shock train is directly dependent on the combustion heat addition sub-sequential to the transverse jet fuel mixing process, the iterative interaction between fuel mixing, combustion heat addition and flow structures are complex with coupling nature. To understand the interactions, the transverse jet penetration depth and the stream-wise length are quantified based on the image processing method detailed in the previous section. The penetration depth is the main injection parameter and the stream-
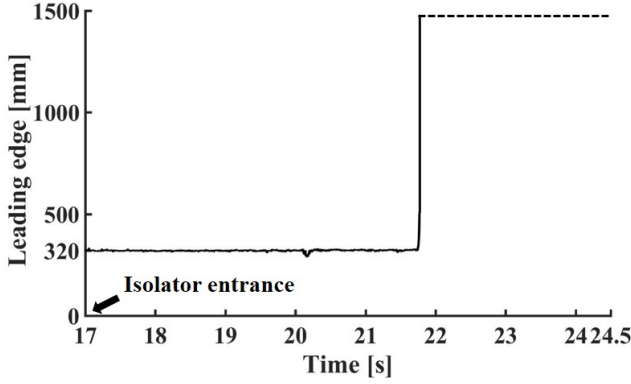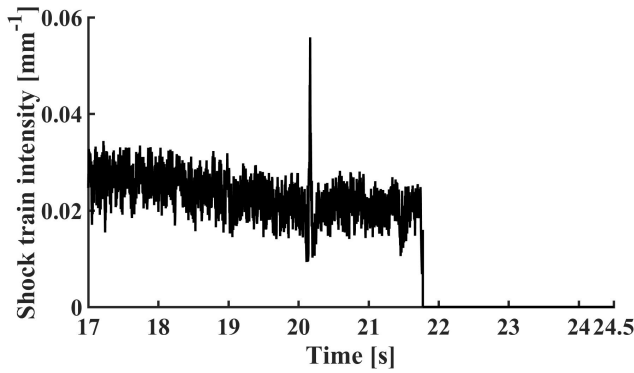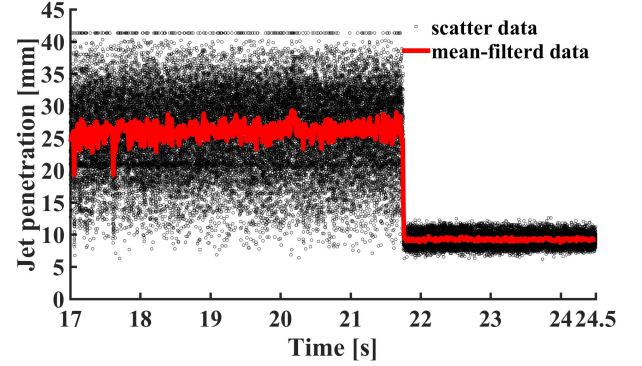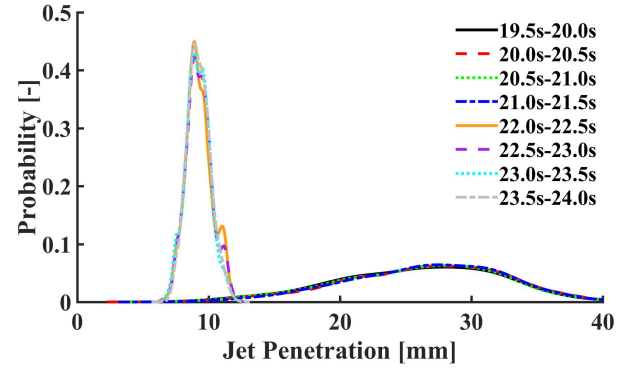
FIG. 19: Time history of shock train leading edge.



FIG. 20: Time history of the pseudo-combustion shock train intensity.



(a)



(b)

FIG. 21: Transient characteristics evolution, time history of (a) jet penetration and (b) corresponding probability distribution during 19.5s-21.5s and 22.0s-24.0s.

wise length is considered as a good indication of the location where the liquid column breaks up, which is critical for the fuel mixing process.

Fig. 21 and Fig. 22 show the time series of the jet penetration depth and liquid length and its temporal probability evolution. Under the ramjet mode, the jet penetration is significantly higher than that of the scramjet mode and is around four times higher in fluctuation level shown as a large spread of pdfs. On the contrary, the jet liquid length is lower under the ramjet mode with a higher level of fluctuation. The jet penetration depth and liquid length are relatively stable under both ramjet and scramjet mode, suggesting the dispersed phase of fuel concentration and mixing efficiency are likely to be independent of the mainstream flow acceleration. This is ensured by the thermal throat of the upstream pseudo-combustion shock train system, of which the intensity decreases, yet its leading edge remains at a fixed location. Since the fuel mass flow rate has been kept constant and the total air mass flow rate decreases during vehicle acceleration, the fuel to air equivalence ratio increases during the flight acceleration. The above mentioned phenomenon results in an ascending trend in the heat released and the thrust under the ramjet mode as shown in Fig. 10a and Fig. 7.

### D.  MODE TRANSITION TRANSIENTS

In previous sections, an ascending trend in the heat released and the thrust under the ramjet mode are observed during acceleration. Detailed discussions are given on the flame and flow dynamics including the pseudo-combustion shock train and crossflow fuel jets performance. We have not answered the question of the triggering mechanism responsible for the ram to scram mode transition and thrust abruption in flight acceleration. To this end, attempts are given below to provide possible explanations.

The high-speed Schlieren and CH* chemiluminescence images of the transient process during mode transition are shown in Fig. 23 for qualitative observation. It is quite obvious from the Schlieren imaging that the ram to scram mode transition process is characterized by flow acceleration, downstream moving and decaying pseudo-combustion shock train from normal to oblique structure until dissipation. For the crossflow fuel injection, the jet penetration depth and liquid length are relatively stable under both ramjet and scramjet mode. Under the ramjet mode, the jet penetration is significantly higher than that of the scramjet mode but the jet liquid length is somehow lower caused by higher combustion-induced back pressure. The observation is consistent with the quantitative
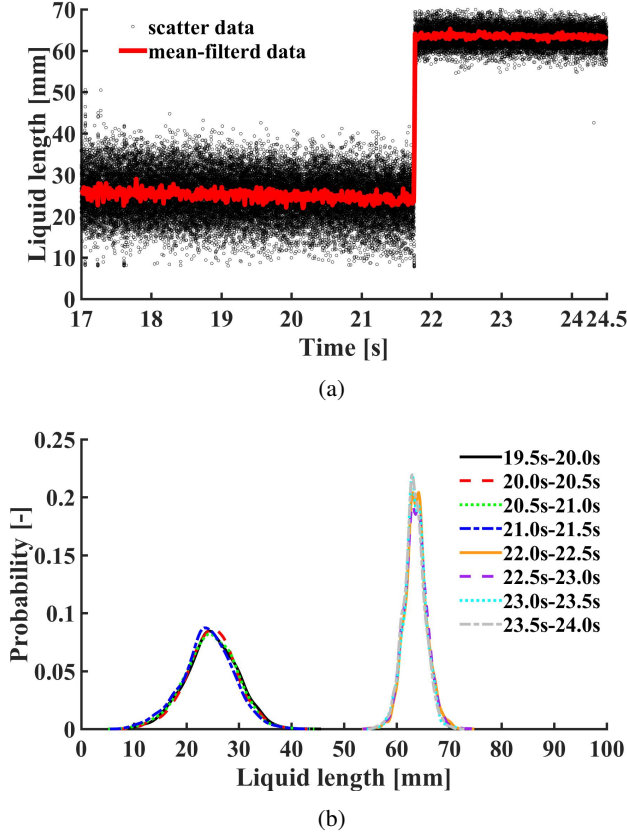
(a)



(b)

FIG. 22: Transient characteristics evolution, time history of (a) liquid length and (b) corresponding probability distribution during 19.5s-21.5s and 22.0s-24.0s.

evaluation in the previous section.

The transient process during mode transition is categorized into four phases and summarized below:

**Phase 1:** The moving pseudo-combustion shock train acts on the fuel jets and reduces the jet penetration depth with enhanced mixing in the near-wall area, resulting in a higher level of fluctuation in combustion.

**Phase 2:** The pseudo-combustion shock train has moved downstream, the energy containing head shock of the pseudo-combustion shock train interacts with the fuel jet. The jet penetration depth decreases significantly with sharp a increase in the liquid length. The flame moves downstream and towards the cavity.

**Phase 3:** The pseudo-combustion shock train dissipates. The supersonic core flow results in flame motion into the cavity.

**Phase 4:** The supersonic core flow completely dominates the diverging duct and is characterized by cavity stabilization combustion.

Simplified illustration of the transient process during mode transition is shown in Fig. 24.

The high repetition rate static wall pressure measurements, the jet penetration and liquid length derived from the previous section, as well as the total heat released in the cavity represented by the integral of CH* chemiluminescence are shown below. The above mentioned four transient phases during mode transition are marked in detail in Fig. 25. The HP-L,HP-M and HP-R represent the high-frequency pressure sensors at the upstream, central and rear edge of the cavity respectively. The locations of the three high frequency pressure sensors are shown in Fig. 4. A higher level of fluctuation in the heat released is observed in Fig. 25a before the observed motion of the pseudo-combustion shock train at 21.75s. Shortly after 21.75s, peaks are observed at the upstream, central and rear edge of the cavity pressure sensor confirming the presence of a moving pseudo-combustion shock train. Consistent with the quantification in the previous section, the jet penetration depth and the liquid length are stable with small fluctuation before interactions with the moving pseudo-combustion shock train.

With the transient process of mode transition detailed above, attempts are given below to provide possible explanations of its triggering mechanism. Referring to Equation 8 in the previous section. The theoretical Mach number based on the quasi-steady analysis is a function of the cross section area of the model combustor. The cross section area usually neglects friction and the effect of thermal flow boundary layer. For simplification, we assume the following relationship taking into account of the thermal flow boundary layer effects.

$$A_{real}(x,t) = A(x) - \delta(x,t) \tag{13}$$

where $\delta(x,t)$ represents the boundary layer thickness at the given location. It has been found that the boundary layer thickness is negatively related to the flow Reynolds number[50], yet, physical understanding and theory of the reacting flow boundary layer thickness is still vacant. At each flight Mach number, it is most likely that a delicate pressure balance has been achieved and sustained between the counteract effects of flow acceleration and heat addition. The pseudo-combustion shock train position is maintained in the isolator under the ramjet mode. The increased flow Mach number and the total temperature lead to variations in boundary-layer thickness, and consequential the cross-sectional area of the model combustor. It is very possible that a sudden variation in the reactive boundary layer upsets the balance between the counteract effects between the flow acceleration and heat addition and results in the pseudo-combustion shock train dynamics and eventually the mode transition. However, currently we could not provide a definite explanation to the triggering mechanism effect due to lack of quantitative experimental method for the reactive boundary layer.

### E.   CONCLUSION

Successful development of the direct-connected transient Flight Trajectory Simulator 1 (FTS-1) at the Institute of Mechanics, Chinese Academy of Sciences enables ground-based simulation of flight acceleration. Kerosene fueled dual-mode
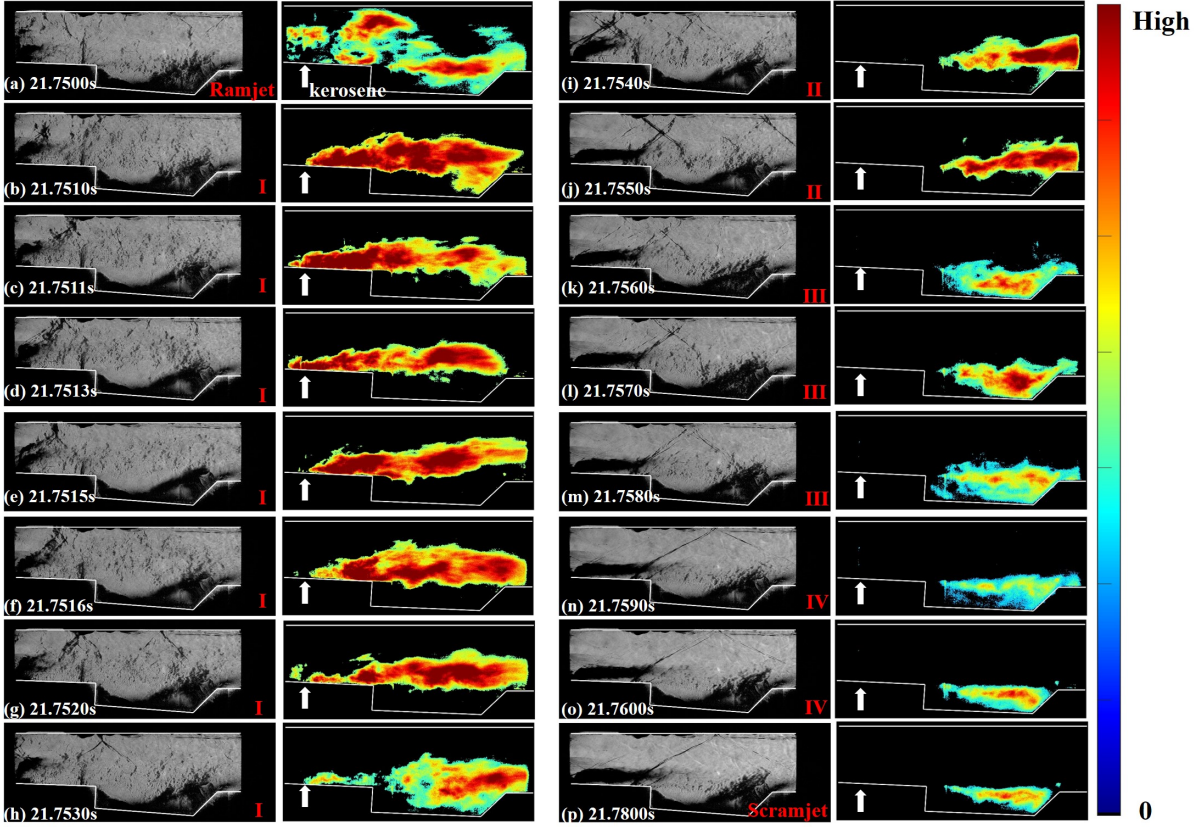
FIG. 23: The high-speed Schlieren and CH* chemiluminescence images from (a) 21.7500s to (p) 21.7800s.
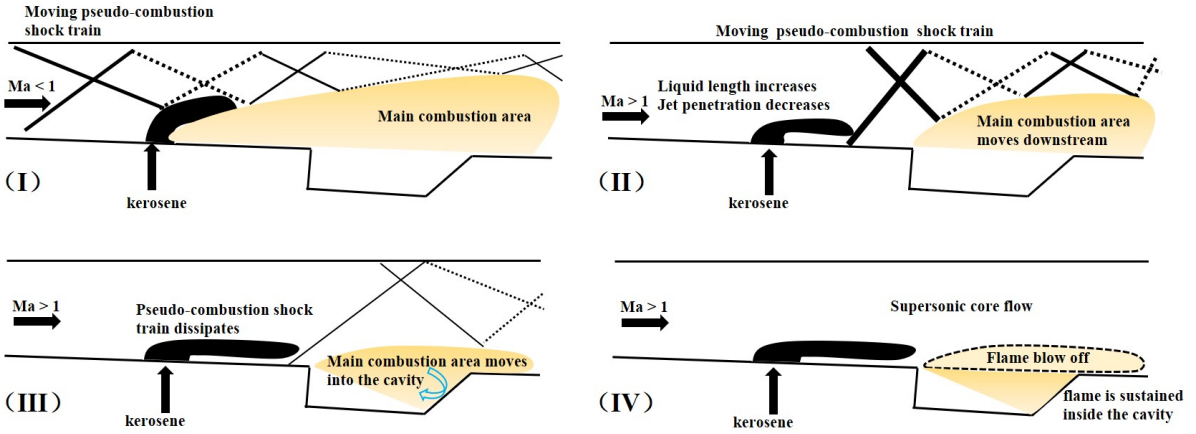


FIG. 24: Illustration of the transient process during mode transition from 21.7500s to 21.7800s.

combustor experiments are designed to study the acceleration-induced mode transition dynamics and transients. The main findings are summarized below.

- Based on the static wall pressure and thrust measurements, for the current simulation of flight acceleration, ramjet mode occurs from 14.5s-21.5s and is followed by mode transition between 21.5s to 22.0s. Sus-

tainable scramjet mode is from 22.0-24.0s until the end of the simulated acceleration at 24.5s. Since the mass flow rate of kerosene fuel has been kept constant, acceleration-induced thrust abruption is observed first time from the ground experiment during mode transition at 21.809s. Generally, the heat released under the ramjet mode shows an ascending trend and appears to
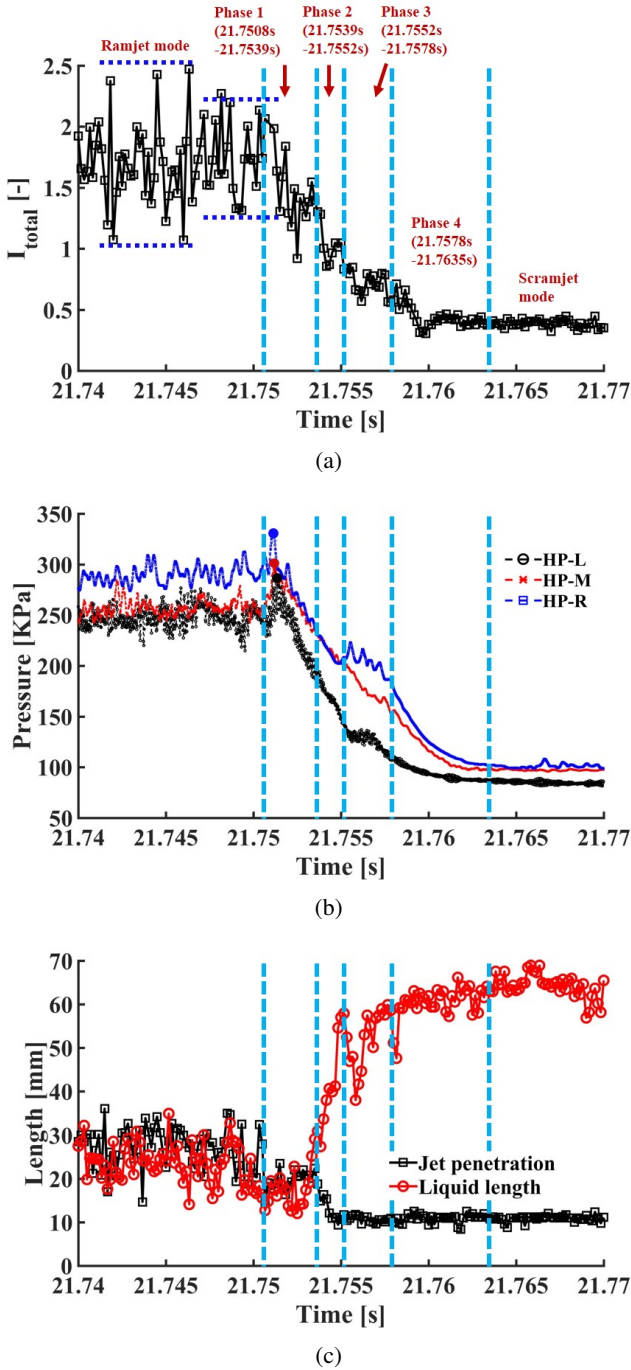
FIG. 25: Transient characteristics evolution in mode transition process, time history of (a) $I_{total}$, (b) high-frequency pressure, (c) jet penetration and liquid length.

be consistent under the scramjet mode during the simulated flight acceleration. The temporal evolution of the probability of $I_{total}$ in each $0.5s$ window shows that the heat released at the ramjet mode is significantly higher than that of the scramjet mode. Under the ramjet mode, the pdf spread of the heat release is about four times of that of the scramjet mode, suggesting strong combus-

tion oscillation under the ramjet mode.

• POD analysis and flame spread angle identification of the CH* chemiluminescence high-speed images are performed. Physical understandings from the two methods are consistent. Significant temporal evolution of turbulent coherent structure is observed under the ramjet mode, which is induced by acceleration-cavity interaction. The flame spreading angle ($\theta$) positively correlates to the mainstream flow velocity ($U$), suggesting the increase of flame propagation rate ($S_T$) is due to both the mainstream acceleration and the acceleration-induced flow transportation. The flame dynamics is characterized as jet wake, cavity stabilized combustion and in-between combustion oscillations. Different from the ramjet mode acceleration, there is little temporal evolution of the turbulent coherent structures under the scramjet mode. The flame spread angle ($\theta$) is near constant, suggesting the flame propagation rate ($S_T$) is purely governed by the mainstream acceleration ($U$). The flame dynamics is characterized as shear layer cavity stabilized combustion with little oscillation.

• Quantitative evaluations of the pseudo-combustion shock train and crossflow fuel jets performance are given of the simulated acceleration. Under the ramjet mode, the jet penetration is significantly higher than that of the scramjet mode and is around four times higher in fluctuation level shown a large spread of pdfs. On the contrary, the jet liquid length is lower under the ramjet mode with a higher level of fluctuation. The jet penetration depth and liquid length are relatively stable under both ramjet and scramjet mode, suggesting the dispersed phase of fuel concentration and mixing efficiency are likely to be independent of the mainstream flow acceleration. This is ensured by the thermal throat of the upstream pseudo-combustion shock train system, of which the intensity decreases, yet its leading edge remains at a fixed location. Since the fuel mass flow rate has been kept constant and the total air mass flow rate decreases during vehicle acceleration, the fuel to air equivalence ratio increases during the flight acceleration. The above mentioned phenomenon results in an ascending and stable trend in the heat released and the thrust under the ramjet and scramjet mode.

• The transient process during mode transition is categorized into four phases based on the behavior of the moving pseudo-combustion shock train. Attempts are given to provide possible explanations of its triggering mechanism. At each flight Mach number, it is most likely that a delicate pressure balance has been achieved and sustained between the counteract effects of flow acceleration and heat addition. The pseudo-combustion shock train position is maintained in the isolator under the ramjet mode. The increased flow Mach number and the total temperature lead to variations in boundary-layer thickness, and consequential the cross-sectional area of the model combustor. It is very possible that a

sudden variation in the reactive boundary layer upsets the balance between the counteract effects between the flow acceleration and heat addition and results in the pseudo-combustion shock train dynamics and eventually the mode transition. However, currently we could not provide a definite explanation to the triggering mechanism effect due to lack of quantitative experimental method for the reactive boundary layer.

## ACKNOWLEDGMENTS

[1] P. L. Moses, V. L. Rausch, L. T. Nguyen, and J. R. Hill. Nasa hypersonic flight demonstrators—overview, status, and future plans. *Acta Astronautica*, 55:619–630, 2004.

[2] J. Hu, W. Bao, and J. Chang. Flame transition in dual-mode scramjet combustor with oxygen piloted ignition. *Journal of Propulsion and Power*, 30(4):1103–1107, 2014.

[3] Q. Liu, D. Baccarella, and T. Lee. Review of combustion stabilization for hypersonic airbreathing propulsion. *Progress in Aerospace Sciences*, 119:100636, 2020.

[4] A. Ben-Yakar, M. G. Mungal, and R. K. Hanson. Time evolution and mixing characteristics of hydrogen and ethylene transverse jets in supersonic crossflows. *Physics of Fluids*, 18(2):026101, 2006.

[5] M. R. Gruber, A. S. Nejadt, T. H. Chen, and J. C. Dutton. Mixing and penetration studies of sonic jets in a mach 2 freestream. *Journal of Propulsion and Power*, 11(2):315–323, 1995.

[6] A. Ben-Yakar and R. K. Hanson. Ultra-fast-framing schlieren system for studies of the time evolution of jets in supersonic crossflows. *Experiments in Fluids*, 32(6):652–666, 2002.

[7] M. B. Sun and Z. W. Hu. Mixing in nearwall regions downstream of a sonic jet in a supersonic crossflow at mach 2.7. *Physics of Fluids*, 30(10), 2018.

[8] A. Oamjee and R. Sadanandan. Effects of fuel injection angle on mixing performance of scramjet pylon-cavity flameholder. *Physics of Fluids*, 32(11), 2020.

[9] A. Pizzaia and T. Rossmann. Effect of boundary layer thickness on transverse sonic jet mixing in a supersonic turbulent crossflow. *Physics of Fluids*, 30(11), 2018.

[10] H. Wang, Z. Wang, M. Sun, and H. Wu. Combustion modes of hydrogen jet combustion in a cavity-based supersonic combustor. *International Journal of Hydrogen Energy*, 38(27):12078–12089, 2013.

[11] A. Ben-Yakar and R. K. Hanson. Supersonic combustion of cross-flow jets and the influence of cavity flame-holders. In *37th Aerospace Sciences Meeting and Exhibit*, 1999.

[12] M. R. Gruber, R. A. Baurle, T. Mathur, and K. Y. Hsu. Fundamental studies of cavity-based flameholder concepts for supersonic combustors. *Journal of Propulsion and Power*, 17(1):146–153, 2001.

[13] K. A. Verma, K. M. Pandey, M. Ray, and K. K. Sharma. Effect of transverse fuel injection system on combustion efficiency in scramjet combustor. *Energy*, 218:119511, 2020.

[14] W. Huang, M. Pourkashanian, L. Ma, D. B. Ingham, S. B. Luo, and Z. G. Wang. Investigation on the flameholding mechanisms in supersonic flows: backward-facing step and cavity flameholder. *Journal of Visualization*, 14(1):63–74, 2011.

[15] R. Masumoto, S. Tomioka, K. Kudo, A. Murakami, K. Kato, and H. Yamasaki. Experimental study on combustion modes in a supersonic combustor. *Journal of Propulsion and Power*, 27(2):346–355, 2011.

[16] M. L. Fotia and J. F. Driscoll. Isolator-combustor interactions in a direct-connect ramjet-scramjet experiment. *Journal of Propulsion and Power*, 28(1):83–95, 2012.

[17] Y. Zhang, B. Chen, G. Liu, B. Wei, and X. Xu. Influencing factors on the mode transition in a dual-mode scramjet. *Acta Astronautica*, 103:1–15, 2014.

[18] W. Shi, Y. Tian, J. L. Le, and F. Zhong. Effect of pilot hydrogen on the formation of dynamic flame in an ethylene-fueled scramjet with a cavity. *Physics of Fluids*, 33(5), 2021.

[19] Y. Tian, W. Shi, F. Zhong, and J. L. Le. Pilot hydrogen enhanced combustion in an ethylene-fueled scramjet combustor at mach 4. *Physics of Fluids*, 33(1), 2021.

[20] Y. Wang, Z. Wang, M. Sun, and H. Wang. Combustion stabilization modes in a hydrogen-fueled scramjet combustor at high stagnation temperature. *Acta Astronautica*, 152:112–122, 2018.

[21] Y. Wang, Z. Wang, M. Sun, H. Wang, and Z. Cai. Effects of fueling distance on combustion stabilization modes in a cavity-based scramjet combustor. *Acta Astronautica*, 155:23–32, 2019.

[22] D. J. Micka, S. M. Torrez, and J. F. Driscoll. Heat release distribution in a dual-mode scramjet combustor - measurements and modeling. In *16th AIAA/DLR/DGLR International Space Planes and Hypersonic Systems and Technologies Conference*, pages 2009–7362, 2009.

[23] S. Nakaya, R. Kinoshita, J. Lee, H. Ishikawa, and M. Tsue. Analysis of supersonic combustion characteristics of ethylene/methane fuel mixture on high-speed measurements of ch* chemiluminescence. *Proceedings of the Combustion Institute*, 37(3):3749–3756, 2018.

[24] H. Wang, Z. Wang, M. Sun, and N. Qin. Combustion characteristics in a supersonic combustor with hydrogen injection upstream of cavity flameholder. *Proceedings of the Combustion Institute*, 34(2):2073–2082, 2013.

[25] Y. Yuan, T. Zhang, W. Yao, X. Fan, and P. Zhang. Characterization of flame stabilization modes in an ethylene-fueled supersonic combustor using time-resolved ch * chemiluminescence. *Proceedings of the Combustion Institute*, 36(2):2919–2925, 2017.

[26] C. C. Rasmussen, J. F. Driscoll, C. D. Carter, and K. Y. Hsu. Characteristics of cavity-stabilized flames in a supersonic flow. *Journal of Propulsion and Power*, 21(4):765–768, 2005.

[27] C. C. Rasmussen, J. F. Driscoll, K. Y. Hsu, J. M. Donbar, M. R. Gruber, and C. D. Carter. Stability limits of cavity-stabilized flames in supersonic flow. *Proceedings of the Combustion Institute*, 30(2):2825–2833, 2005.

[28] C. C. Rasmussen, S. K. Dhanuka, and J. F. Driscoll. Visualization of flame-holding mechanisms in a supersonic combustor using plif. *Proceedings of the Combustion Institute*, 31(2):2505–2512, 2007.

[29] C. Liu, Z. Wang, M. Sun, H. Wang, and P. Li. Characteristics of a cavity-stabilized hydrogen jet flame in a model scramjet combustor. *AIAA Journal*, 57(4):1624–1635, 2019.

[30] W. H. Heiser, D. T. Pratt, D. H. Daley, and U. B. Mehta. *Hypersonic airbreathing propulsion*. AIAA Education Series. Washington, D.C., 1994.

[31] S. J. Laurence, S. Karl, J. M. Schramm, and K. Hannemann. Transient fluid-combustion phenomena in a model scramjet. *Journal of Fluid Mechanics*, 722:85–120, 2013.

[32] A. R. Wieting. Exploratory study of transient upstart phenomena in a three-dimensional fixed-geometry scramjet engine. Report, Washington, D.C., 1976.

[33] P. E. Rodi, S.. Emami, and C. A. Trexler. Unsteady pressure behavior in a ramjet/scramjet inlet. *Journal of Propulsion and Power*, 12(3):486–493, 1996.

[34] J. L. Wagner, K. B. Yuceil, A. Valdivia, N. T. Clemens, and D. S. Dolling. Experimental investigation of unstart in an inlet/isolator model in mach 5 flow. *AIAA Journal*, 47(6):1528–1542, 2009.

[35] T. Shimura, T. Mitani, N. Sakuranaka, and M. Izumikawa. Load oscillations caused by unstart of hypersonic wind tunnels and engines. *Journal of Propulsion and Power*, 14(3):348–353, 1998.

[36] S. O'Byrne, M. Doolan, S. R. Olsen, and A. F. P. Houwing. Analysis of transient thermal choking processes in a model scramjet engine. *Journal of Propulsion and Power*, 16(5):808–814, 2000.

[37] M. L. Fotia and J. F. Driscoll. Ram-scram transition and flame/shock-train interactions in a model scramjet experiment. *Journal of Propulsion and Power*, 29(1):261–273, 2013.

[38] G. A. Sullins, D. A. Carpenter, M. W. Thompson, F. T. Kwork, and L. A. Mattes. A demonstration of mode transition in a scramjet combustor. In *AIAA /ASME/SAE/ASEE 27th Joint Propulsion Conference*, 1991.

[39] G. A. Sullins. Demonstration of mode transition in a scramjet combustor. *Journal of Propulsion and Power*, 9(4):515–520, 1993.

[40] C. Zhang, J. Chang, J. Zhang, W. Bao, and D. Yu. Effect of continuous mach number variation of incoming flow on ram–scram transition in a dual-mode combustor. *Aerospace Science and Technology*, 76:433–441, 2018.

[41] Y. Hardalupas, C. S. Panoutsos, and A. M. K. P. Taylor. Spatial resolution of a chemiluminescence sensor for local heat-release rate and equivalence ratio measurements in a model gas turbine combustor. *Experiments in Fluids*, 49(4):883–909, 2010.

[42] N. Otsu. A threshold selection method from gray-level histograms. In *IEEE TRANSACTIONS ON SYSTEMS MAN AND CYBERNETICS*, volume 9, pages 62–66, 1979.

[43] L. Sirovich. Turbulence and the dynamics of coherent structures. i. coherent structures. *Quarterly of Applied Mathematics*, 45(3):561–571, 1987.

[44] A. Chatterjee. An introduction to the proper orthogonal decomposition. *Current science*, 78(7):808–817, 2000.

[45] H. Chen, D. L. S. Hung, M. Xu, H. Zhuang, and J. Yang. Proper orthogonal decomposition analysis of fuel spray structure variation in a spark-ignition direct-injection optical engine. *Experiments in Fluids*, 55(4):1–12, 2014.

[46] T. B. Steva, C. P. Goyne, R. D. Rockwell, D. Cresci, and J. W. Osborne. Comparison of a direct-connect and freejet dual-mode scramjet. *Journal of Propulsion and Power*, 31(5):1380–1392, 2015.

[47] W. Huang, Z. B. Du, L. Yan, and R. Moradi. Flame propagation and stabilization in dual-mode scramjet combustors: A survey. *Progress in Aerospace Sciences*, 101:13–30, 2018.

[48] D. J. Micka. *Combustion Stabilization, Structure, and Spreading in a Laboratory Dual-Mode Scramjet Combustor*. Phd thesis, The University of Michigan, 2010.

[49] J. R. Hutzel, D. D. Decker, R. G. Cobb, P. I. King, M. J. Veth, and J. M. Donbar. Scramjet isolator shock train location techniques. In *49th A-IAA Aerospace Sciences Meeting including the New Horizons Forum and Aerospace Exposition*, volume 2011-402, 2011.

[50] S Hermann and G Klaus. *Boundary-Layer Theory*. Springer, Berlin, 2017.